

High-Pressure Studies of Correlated Electron Systems

Pau Jorba, Alexander Regnat, Anh Tong, Marc Seifert, Andreas Bauer, Michael Schulz, Christian Franz, Astrid Schneidewind, Stefan Kunkemöller, Kevin Jenni, Markus Braden, Andre Deyerling, Marc A. Wilde, James S. Schilling, and Christian Pfleiderer*

Tuning the electronic properties of transition-metal and rare-earth compounds by virtue of changes of the crystallographic lattice constants offers controlled access to new forms of order. The development of tungsten carbide (WC) and moissanite Bridgman cells conceived for studies of the electrical resistivity up to 10 GPa, as well as bespoke diamond anvil cells (DACs) developed for neutron depolarization studies up to 20 GPa is reviewed. For the DACs, the applied pressure changes as a function of temperature in quantitative agreement with the thermal expansion of the pressure cell. A setup is described that is based on focusing neutron guides for measurements of the depolarization of a neutron beam by samples in a DAC. The technical progress is illustrated in terms of three examples. Measurements of the resistivity and neutron depolarization provide evidence of ferromagnetic order in SrRuO_3 up to 14 GPa close to a putative quantum phase transition. Combining hydrostatic, uniaxial, and quasi-hydrostatic pressure, the emergence of incipient superconductivity in CrB_2 is observed. The temperature dependence of the electrical resistivity in CeCuAl_3 is consistent with emergent Kondo correlations and an enhanced coupling of magneto-elastic excitations with the conduction electrons at low and intermediate temperatures, respectively.

1. Introduction

In strongly correlated electron systems, the magnetic and electronic properties are intimately connected with the crystallographic structure. Subtle changes in the lattice constants or symmetries may lead to fundamental changes in the electronic properties and to the emergence of non-Fermi liquid behavior near quantum criticality,^[1–3] unconventional superconductivity,^[4–6] or novel forms of order.^[7,8] The application of uniaxial, or hydrostatic pressure, or a combination thereof, represents the perhaps best-controlled tool for tuning the underlying crystallographic lattice constants.


Experimentally, high pressures are generated by means of pressure cells. These are typically composed of a metallic body that permits to apply a load to a relatively small sample space but also drastically limits the range of experimental methods and the accessible parameter range. In turn, a

large variety of designs of pressure apparatus has been developed to address specific scientific questions.^[9] Noticeable examples

P. Jorba, A. Regnat, A. Tong, M. Seifert, A. Bauer, C. Franz, A. Deyerling, M. A. Wilde, J. S. Schilling, C. Pfleiderer
 Physik-Department
 Technical University of Munich
 D-85748 Garching, Germany
 E-mail: pau.jorba@ph.tum.de

M. Seifert, M. Schulz, C. Franz
 Heinz Maier-Leibnitz Zentrum (MLZ)
 Technical University of Munich
 D-85748 Garching, Germany

A. Bauer, M. A. Wilde, C. Pfleiderer
 Centre for Quantum Engineering (ZQE)
 Technical University of Munich
 D-85748 Garching, Germany

 The ORCID identification number(s) for the author(s) of this article can be found under <https://doi.org/10.1002/pssb.202100623>.

© 2022 The Authors. physica status solidi (b) basic solid state physics published by Wiley-VCH GmbH. This is an open access article under the terms of the Creative Commons Attribution License, which permits use, distribution and reproduction in any medium, provided the original work is properly cited.

DOI: 10.1002/pssb.202100623

C. Franz, A. Schneidewind
 Jülich Centre for Neutron Science (JCNS) at Heinz Maier-Leibnitz Zentrum (MLZ)
 Forschungszentrum Jülich GmbH
 D-85748 Garching, Germany

S. Kunkemöller, K. Jenni, M. Braden
 II. Physics Institute
 University of Cologne
 D-50937 Cologne, Germany

J. S. Schilling
 Department of Physics
 Washington University
 St. Louis, MO 63130, USA

C. Pfleiderer
 Munich Centre for Quantum Science and Technology (MCQST)
 Technical University of Munich
 D-85748 Garching, Germany

include Bridgman cells with large tungsten carbide (WC) anvils for electrical transport measurements and diamond anvil cells (DACs) with small diamond anvils that are capable of reaching record-high pressures of up to 600 GPa.^[10]

In this review, we report the development of high-pressure measurement techniques achieved in the past decade. This development includes the design of Bridgman cells using anvils made of moissanite and polycrystalline diamond (PCD), the design of three different DACs, the possibility for in situ pressure determination using ruby fluorescence, and a setup for neutron depolarization measurements under high pressure. In addition, we showcase the potential of these high-pressure techniques in terms of studies on three different materials. First, in the itinerant-electron ferromagnet SrRuO₃, the suppression of ferromagnetic order under high pressure was investigated by means of neutron depolarization and electrical resistivity measurements. Second, in the itinerant antiferromagnet CrB₂, the emergence of incipient superconductivity under quasi-hydrostatic pressure was demonstrated by means of electrical resistivity measurement. Third, in the rare-earth compound, CeCuAl₃ the evolution of the magneto-elastic coupling under pressure was addressed by means of electrical resistivity measurements.

2. Experimental Methods

2.1. Bridgmann Cells

Quasi-hydrostatic pressure may be applied using Bridgman cells. These cells were characterized by a relatively large sample space while being compact enough to fit into most cryostats. This type of pressure cell, where large tungsten carbide (WC) anvils were pressed against each other with very large loads, can reach pressures as high as 10 GPa.^[11] More importantly, Bridgman cells were almost exclusively used for transport measurements, as the anvils were opaque impeding any optical access. Additionally, although nonmagnetic WC can be manufactured, these so-called nonmagnetic materials typically still carry a small magnetic moment at low temperatures.

It was attempted to replace the WC anvils with large synthetic moissanite anvils to increase the accessible pressure range, and at the same time provide optical access to the sample. With a hardness of 3000 on the Knoop scale, synthetic moissanite (hexagonal silicon carbide) was harder than sapphire (2000) and cubic zirconia (1370) but softer than diamond (5700 to 10 400).^[12] Large, gem-quality, single-crystal synthetic moissanite anvils were available commercially. **Figure 1** shows the design and the different parts of the modified Bridgman cell that was built. The cell parts were made of hardened copper beryllium, while the moissanite anvil was kept in place with a brass ring.

However, this attempt was unsuccessful since the anvils repeatedly failed, breaking into small pieces under small applied loads. Many reasons may explain this situation. The two main lessons that have been learned from this attempt may be summarized as follows. First, although moissanite is an extremely hard material upon compression, only surpassed by diamond, it is far from being tough and can break easily when stress is accumulated on a small surface or at an edge. Therefore, the alignment between the two

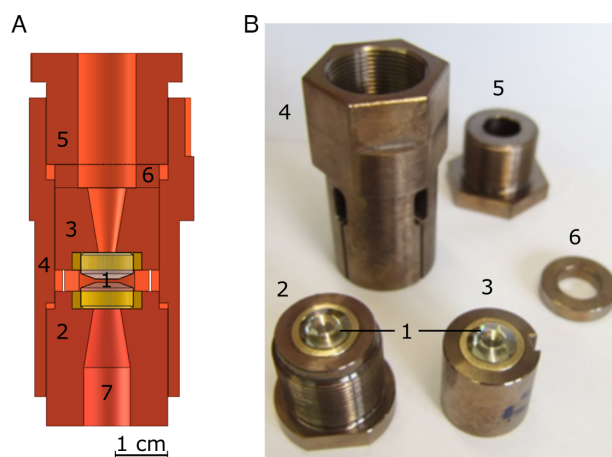


Figure 1. Bridgman cell with moissanite anvils. A) Section view of the cell model. Large moissanite anvils (1) are mounted on the bottom nut (2) and the piston (3). The bottom nut is screwed into the main cell body (4) while the piston slides into it. Load is applied with a hydraulic press on the piston, and locked in place with the locking nut (5). A large ring (6) is used as a washer to decrease the transmission of torque. Apertures in the cell body (7) allow for optical access to the back of the anvils on both sides. B) Photograph of the cell with the different parts.

anvils must be very well adjusted. To maintain this alignment, the piston–cylinder fit of the cell should be very tight.

Second, as already known for diamonds but also applicable to moissanite, the larger the anvil the higher the probability that a flaw of sufficient size may exist leading to failure.^[13] The anvils were made identical in dimensions matching the WC anvils originally used in these cells with a diameter of 10 mm at the base, and a culet size of 3.5 mm. This was much larger than the typical moissanite/diamond anvils used in high-pressure experiments.

To overcome some of these difficulties, the design and manufacturing of the Bridgman cells were improved. In favor of reaching higher pressures, supported PCD anvils were used. The piston–cylinder fit of the pressure cell was also improved, keeping the difference of the diameter between the two parts as low as possible. The cylinder in the cell body was made with great precision using honing drills. The piston was manufactured slightly bigger in diameter than the cylinder and material was carefully ground away until a satisfactory fit was obtained. Additionally, we increased the length of engagement of the piston and cylinders from 15 to 36 mm to prevent the piston from wobbling inside the housing. **Figure 2** shows a drawing of the new design and a picture comparing it to the previous design.

The capability of big anvils to sustain larger loads may be improved by means of supported anvils. The operating principle of supported anvils was to force-fit an anvil with slightly conical sides (about 1°) into a matching steel ring of slightly smaller dimension. This so-called interference-fit of ≈1% applied inward-acting radial stress that strengthened the anvil, allowing it to reach far higher pressures than otherwise achievable without breaking.^[14] The experience with moissanite anvils has shown that this material is rather vulnerable to shear stress. Given the large costs of diamonds of the required size, it was decided to use PCD as an anvil material. This is a sintered material made of a fine diamond powder in combination with a cobalt binder.

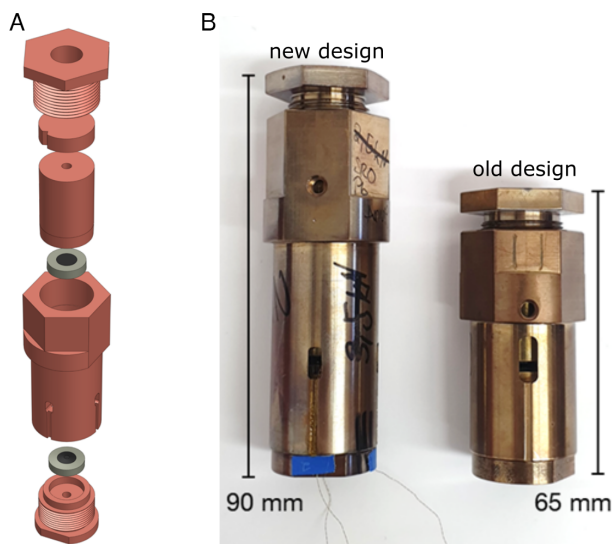


Figure 2. Bridgman cell with polycrystalline diamond (PCD) anvils. A) Drawing of the different cell parts. B) Photograph of the new cell with PCD anvils with an improved piston-cylinder fit compared to the shorter cell used previously.

The anvils used can be seen in **Figure 3**. They are composed of an inner PCD core and an outer shell of WC following a successful design by Ullrich.^[15]

Despite not allowing optical access to the sample, PCD anvils have proven to be much more reliable and have allowed us to perform electrical transport experiments at pressures exceeding 10 GPa. So far no anvil has failed, as experiments are usually terminated when electrical contacts to the sample are lost. Improvements in the sample loading technique promise to mitigate this problem.

2.2. Diamond Anvil Cells

Three DAC were designed and built following essentially the guidelines reported in a comprehensive article by Dunstan and Spain on the principles, design, and construction of DACs.^[13] The cell body had two main roles. It applied a compressing force between the anvils and it aligned the anvils such

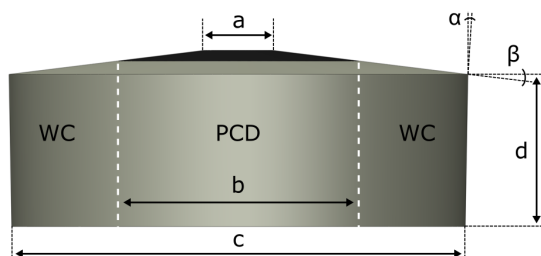


Figure 3. Drawing of the PCD anvil. The anvil is composed of a PCD core (black) of diameter $b = 7.6$ mm with a WC support ring (gray) with $c = 13.2$ mm. The culet dimension is $a = 2$ mm and the height $d = 4.4$ mm. The anvil side has a slight conical shape with $\alpha = 1^\circ$ and the pavilion angle is $\beta = 7^\circ$.

that the culet faces were parallel (tilt alignment) and concentric (xy alignment). A large variety of designs and construction materials were available, of which the best choice may differ subject to the specific experiment. For studies, the cells needed to be non-magnetic, suitable for very low temperatures, small enough to fit inside most cryostats (less than 30 mm diameter), and still able to reach pressures up to 15 GPa.

A so-called “standard design” was chosen as it is simple and offers very good performance. The anvils had a diameter between 3 and 4 mm and a height between 2.2 and 2.5 mm. One of the most critical dimensions of an anvil concerns the culet diameter—the flat top of the anvil that withstands the highest stress. Smaller culet diameters allow for higher pressures but also limit the available sample space. Consequently, it is typically most advantageous to choose the largest culet size that permits to reach the pressure range of interest. Dunstan and Spain propose a formula,^[13] generally accepted in the high-pressure community, which gives the maximum achievable pressure with a DAC for a given culet diameter (d) in usual conditions

$$P_{\max}(\text{GPa}) = \frac{12.5}{(d(\text{mm}))^2} \quad (1)$$

To avoid anvil failure, it is common practice to stay 20% below this value. A culet diameter of 0.8 and 0.5 mm should, therefore, be sufficient to reach 15 and 40 GPa, respectively.

Both diamond and moissanite anvils were used. Unlike natural diamonds, which were cut with either 8 or 16 facets, moissanites were cut with a much larger number of facets and then polished, rendering them seemingly cylindrical. At first, only moissanite anvils were purchased. As further experiments required us to reach higher pressures, natural diamonds were used. Synthetic moissanite anvils were more prone to failure than diamonds, especially in presence of shear forces. Pressures as high as 40 GPa may be reached when using large moissanite anvils that are strengthened with a support ring made of tool steel.^[14] However, this approach requires a significant experimental accuracy in the design and manufacture of the different cell parts. Diamond anvils were less forgiving of design flaws or inexperienced users.

The maximum achievable pressure with moissanite anvils is significantly lower than what is predicted by Equation (1) due to the lower material strength. Taking into account anvil failures, diamond becomes more cost-effective than moissanite, and therefore was the chosen anvil material henceforth.

When studies at low temperatures were intended, copper-beryllium (Cu-Be) is the most common material for the cell body. It is easy to machine in its unhardened state, shows great mechanical properties (similar to stainless steel) after age hardening, is nonmagnetic, and shows a thermal conductivity below 100 K that is at least one order of magnitude higher than in stainless steel.

To generate a force between the anvils, the two most common solutions were hydraulic/pneumatic drive and direct screw drive. Screw-driven cells fit the needs best as they do not require the integration of a large gas membrane and hence allowed for a compact design. As the main drawback, these cells have to be removed from the cryostat to change the pressure at room temperature. Additionally, the pressure might change upon cooling.

Fortunately, these changes happen in a controlled and largely reproducible way. Below 100 K, where most of the magnetic states under investigation emerge, changes of pressure are typically negligible.^[16,17]

Using the same material for the loading screws and the cell body should be avoided, as the friction coefficient between identical materials tends to be large, resulting in cold-working. Therefore, titanium grade 5 (Ti-6Al-4V) was used for the screws. This material is nonmagnetic and has mechanical properties comparable to steel. Moreover, titanium has a smaller thermal expansion coefficient than steel which proves useful for limiting the pressure change under cooling. When the load was applied by tightening the screws, the strain on the thread parts was much larger as compared to when they were used to keep the load in place. This substantially reduced the maximum load that should be applied to the screws. By using four screws, a maximum load capacity of around 8 and 14 kN was achieved for M3 and M4 screws, respectively.

Anvil seats made of nonmagnetic WC were used in all designs. The anvils were glued to the anvil seats using low-temperature curing composite glue (stycast). WC anvil seats were able to withstand higher loads without deformation and further redistributed the load on a larger surface, reducing the risk of deforming the cell body. This practice also allowed for easy reuse of the cell body when the anvils are damaged. To provide optical access to the sample, the anvil seats had an axial aperture, usually cone-shaped with a large opening angle.

In **Figure 4A**, depiction of the cross-section and a photograph of each cell are shown. The outer body shape was based on a cylinder where four faces have been milled out in the sides to allow sample holders and thermometers to be mounted easily. The cells were shown according to increasing complexity. Cell 1, with 22 mm diameter and 34 mm height, was designed to fit in a Physical Property Measurement System (PPMS) from Quantum Design. In this cell, four M3 screws were used to apply the load. These screws proved to be insufficient, showing substantial wear after repeated use. Only lateral (xy) alignment of the anvils was possible, as ensured by four M2 brass set screws. The tilt alignment between the diamonds relied on the machining accuracy of the different parts. Unfortunately, sufficient accuracy of the components was not reached. This cell proved to be prone to anvil failure and only very low pressures were achieved.

The second design, cell 2, was larger with a 30 mm radius and 35 mm height. This time four M4 hexagonal socket screws were used to apply the load, proving to be sufficiently sturdy as no damage could be seen after repeated use. As its main advancement, this cell accommodated a hemispherical rocker adjusted by three M2 brass screws. The hemisphere could be tilted a few degrees in any direction by adjusting these three screws. The advantage of this construction was that it allowed one to adjust the parallelism of the anvils without applying load on the adjustment screws. Moissanite anvils with 0.8 mm culet suggested a maximum of 6 GPa, but a record pressure of 9 GPa was achieved.

The third design, cell 3, was comparable in dimension to the second design with a diameter of 30 mm and a height of 33 mm. This design retained some features of the previous designs, such as the xy aligning mechanism, but instead of using a piston-cylinder fit, three titanium M4 dowel pins were used to ensure

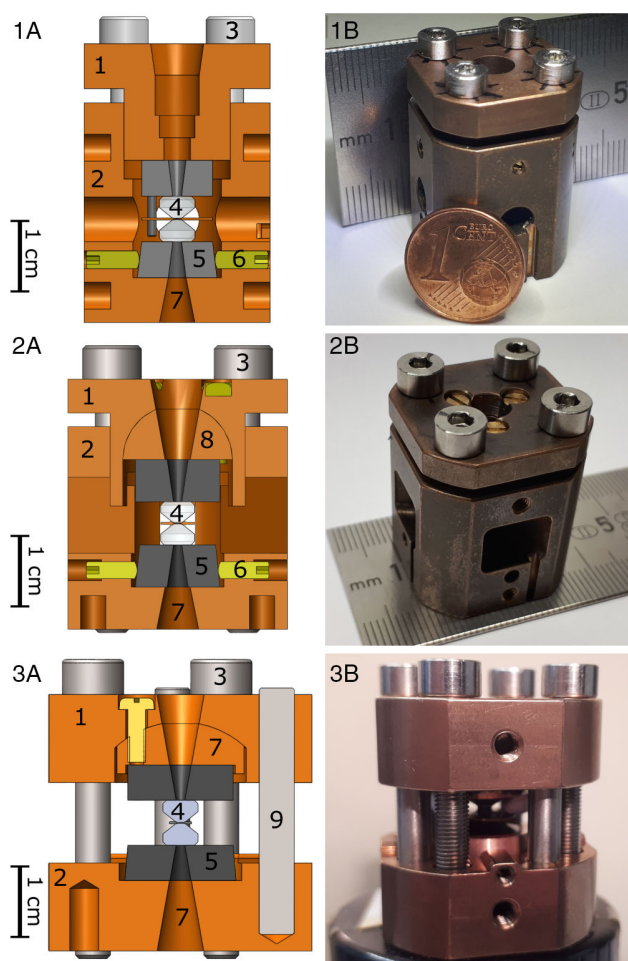


Figure 4. Three diamond anvil cell (DAC) designs. A) Depiction of the cross-section. B) Photograph of the assembled DAC. 1A, 1B: Smallest cell with a piston-cylinder fit between the upper cell body (1) and the bottom cell body (2). M3 titanium screws (3) apply the load which is transmitted to the tip of the diamond (or moissanite) anvils (4) glued on top of tungsten carbide (WC) anvil seats (5). Aligning screws (6) are used to adjust the relative xy position of the anvils. A conical aperture in the cell body (7) provides access to the back of the anvils from both sides. 2A, 2B: Larger design with the same piston-cylinder fit, where M4 screws (3) are used to apply the load. Here, a hemispherical rocker (8) permits a tilt alignment between the anvils. 3A, 3B: The design is similar in size as the previous one also using M4 screws (3) with an improved hemispherical rocker (7). Here, a system of three titanium guide pins (9) is used to keep the two parts of the cell body parallel with respect to each other.

the parallel alignment of the cell body. In a piston-cylinder fit, the applied load on the piston leads to Poisson expansion which puts the piston at risk of jamming into the cylinder if machined too tight. This risk of jamming was avoided by the new design, as no load is applied to the pins, allowing for a much tighter fit between the pins and the cell body.

Further improvements were also implemented in this third design. First, the hemispherical rocker was constructed such that the center of the sphere and the tip of the anvils coincided. This change made the anvil alignment procedure much easier as the tilt and the xy alignment were decoupled. Another significant

change is the use of M4 fine threaded screws to apply the load. These screws allowed for a finer tuning of the pressure and a smaller torque was needed to apply the same load. A copper layer of a few micrometers thickness was sputtered on the anvil seats before attaching the anvils on top. This soft layer between the anvil seats and the anvils served to improve the durability of the anvils by helping to redistribute any local stress by imperfections of the surfaces. Finally, the Cu–Be parts were treated with an etching solution that removed the outer oxide layer appearing after the heat aging treatment.

The third cell design has proven to be very reliable. No attempt on reaching the highest possible pressure has been performed yet, but pressures up to 17 GPa were reached using 0.5 mm culet diamond anvils. It is clear that the improvement in the guiding mechanism was crucial. Each pair of bottom and top parts of these cells are unique and match each other. The two parts were machined together to ensure that the pinholes are perfectly aligned. The holes were drilled with a slightly smaller diameter than the pins before each pin was polished until a perfect fit was reached. The new design also allowed for a much easier access to the sample area from the sides of the pressure cell. Further technical details on the design and utilization of these pressure cells can be found in Ref. [18].

2.3. Pressure Determination

In DACs, pressure is commonly determined by means of ruby fluorescence taking advantage of the optical access. The pressure was calculated from the wavelength shift of the R1 photoluminescence line of a ruby crystal placed inside the sample space. An excellent review of this technique has been reported by Syassen.^[19] The linear ruby scale originally proposed by Piermarini et al.^[20] was confirmed by Syassen to be valid to pressures up to 20 GPa. The pressure increase (ΔP) is directly proportional to the wavelength shift ($\Delta\lambda$) as

$$\frac{\Delta P}{\Delta\lambda} = 2.746 \pm 0.014 \text{ GPa nm}^{-1} \quad (2)$$

For the studies, a compact photoluminescence setup with a solid-state laser and a small high-resolution spectrometer was built. A camera and an optical lens were used to monitor the sample space and to align the ruby crystals with the laser.^[21] A typical ruby spectrum is shown in **Figure 5**. Ruby fluorescence was characterized by two lines, R1 and R2. The position of the R1 and R2 lines, as well as their full-width-at-half-maximum (FWHM) were obtained by fitting the sum of two pseudo-Voigt functions. Using Equation (2), the pressure was calculated from the wavelength shift of the R1 line as it is more intense than the R2 line and the latter loses its intensity at low temperatures. Moreover, the cell temperature was also measured, as the R1 and R2 lines also shift with temperature.^[19]

In screw-driven DACs, the pressure may change significantly as a function of temperature.^[16,17] Therefore, the pressure is ideally determined in situ, which becomes challenging when standard cryostats are used that lack a built-in optical access. Alternatively, the pressure at low temperatures is determined at room temperature prior to each measurement and extrapolated to the expected low-temperature value. This approach

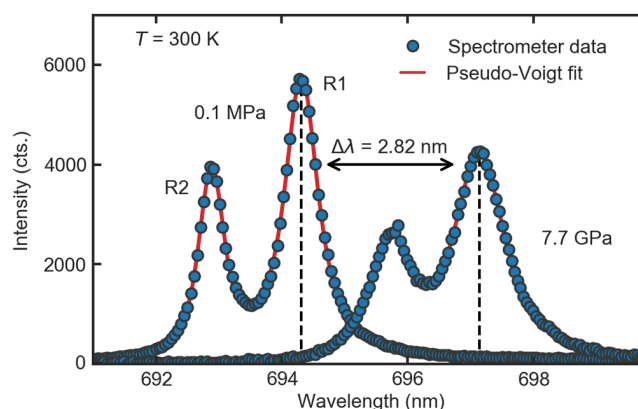


Figure 5. Ruby fluorescence spectra obtained at ambient pressure (0.1 MPa) and inside a loaded pressure cell (7.7 GPa). The spectrum is characterized by the R2 and R1 lines. The position of the R1 lines (dashed line) is determined by fitting the sum of two pseudo-Voigt functions. The pressure may be inferred from the wavelength shift of the R1 line.

motivated the determination of the pressure change of the DACs we constructed (see Figure 4).

For this purpose, a dedicated setup was constructed that allowed us to measure ruby photoluminescence inside the pressure cells as a function of temperature. Details of this setup are shown in **Figure 6**. A sample stick of a variable temperature insert (VTI) from Oxford Instruments was customized and a cryogenic-compatible fiber optic was added. The pressure cell was mounted at the bottom of the sample stick. With the help of a small collimator, the sample space of the pressure cell was coupled to the standard photoluminescence device through multimode fiber optics. The VTI was installed inside a standard helium cryostat. A cernox thermometer directly attached to the

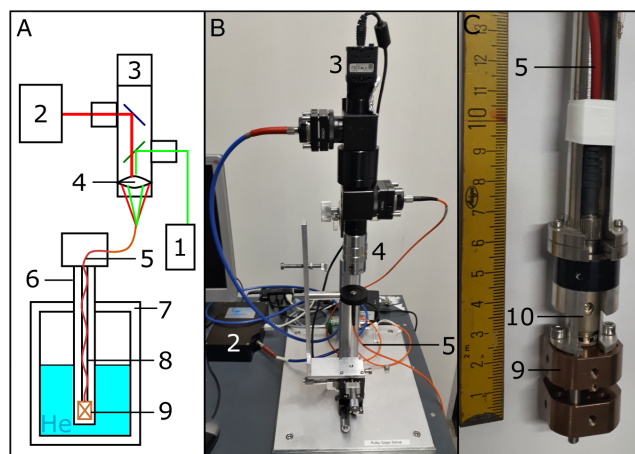


Figure 6. Low-temperature photoluminescence setup. A) Schematic drawing with the components: solid-state laser (1), spectrometer (2), charge-coupled device (CCD) camera (3), optical lens (4), fiber optic (5), variable temperature insert (VTI) (6), wet cryostat (7), sample stick (8), and pressure cell (9). B) Picture detailing the coupling of the photoluminescence setup with the fiber optic. C) Picture of the end of the sample stick, where a collimator (10) is used to optically couple the fiber optics (5) to the pressure cell (9).

pressure cell was used to measure the temperature. Further details on this setup may be found in Ref. [22].

The setup was not suited for in situ pressure determination with a sample in the pressure cell. Only when the sample space was fully loaded with ruby crystals, a measurable signal was obtained through the sample stick. The signal was nonetheless sufficient for characterizing the change of pressure as a function of temperature. The cells were loaded to a given pressure at room temperature. Subsequently, they were cooled to 10 K and heated to room temperature while the ruby luminescence lines were measured every 50 K. Due to the large losses, the fluorescence spectra required an integration time of 180 s and appropriate background subtraction. The sum of two pseudo-Voigt functions was used to fit the spectra and infer the wavelengths of the R1 and R2 lines. The width of the lines decreases at lower temperatures making it easier to detect them as they become sharper.

The wavelengths of the R1 and R2 ruby lines change both with pressure and temperature. The shift of the frequency as a function of temperature $\nu(T)$ for R1 can be calculated as

$$\nu(T) = \nu_0 - \alpha_\nu N \left(\frac{T}{\Theta_\nu} \right) \quad (3)$$

with

$$N \left(\frac{T}{\Theta_\nu} \right) = \frac{1}{\exp(\Theta_\nu/T) - 1} \quad (4)$$

where $\nu_0 = 14421.9 \text{ cm}^{-1}$, $\alpha_\nu = 76.6 \text{ cm}^{-1}$, and $\Theta_\nu = 482 \text{ K}$.^[19] Since the shifts in pressure and temperature are independent of each other,^[23] it was sufficient to calculate the temperature shift of the ruby line at ambient pressure using Equation (3), followed by the computation of the pressure from the wavelength shift between the measured value and the computed value according to Equation (2).

The characterization of the second pressure cell from Figure 4 is shown in Figure 7. The pressure was tracked during a cooling and heating cycle for three different initial pressures. The same trend is observed for the different pressures. When cooling, the pressure increased essentially linearly until it reached a plateau between 100 and 50 K. When warming the pressure cell, the pressure remained constant at first between 10 and 50 K before starting to decrease. Small discrepancies between decreasing and increasing temperature are observed, including a slightly higher pressure at room temperature following a full thermal cycle. When looking at the relative change in pressure, from 300 K to base temperature, it decreases with increasing pressures, nominally changing by 25% at 1.7 GPa, 18% at 2.5 GPa, and 15% at 4.5 GPa.

A rather simple explanation for this behavior may be sought in the thermal expansion. When the cell is cooled down, the different rates of thermal contraction of the various parts of the cell body lead to changes in the load applied on the anvils. Knowing the thermal expansion with respect to the temperature of the different materials and the exact dimensions of the cell, one can compute how the different elements of the pressure cell will contract. As the thermal expansion coefficients change linearly with an applied load within the elastic limit,^[24] the change of

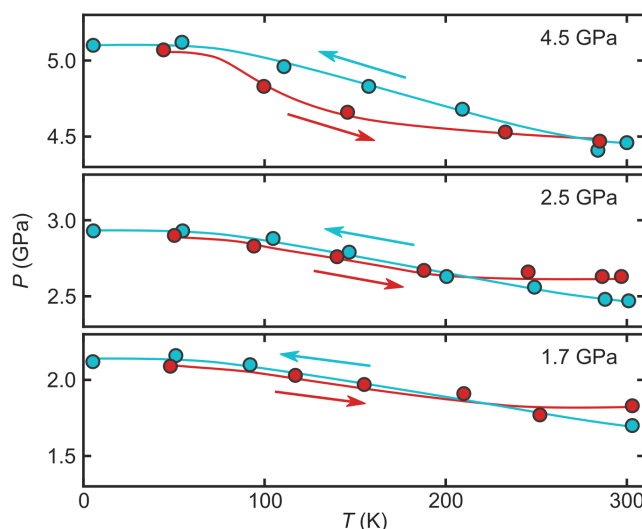


Figure 7. Pressure change upon cooling of the second pressure cell shown in Figure 4. Each panel shows the pressure values during the cooling (blue) and heating (red) cycles for 3 different initial pressures 1.7, 2.5, and 4.5 GPa. Lines are guides to the eye.

pressure under cooling is expected to be similar under different loads and it should decrease for increasing loads.

Figure 8 shows the temperature dependence of the relative difference between the change in length of cell parts that are under tension and the parts that are in compression (as illustrated in Figure 9) as the cell is cooled down. Alongside, the relative change in pressure upon cooling is shown as measured in the characterization experiment of Figure 7. An arbitrary normalization value was applied to the relative change of the length difference between the cell parts arising from the thermal

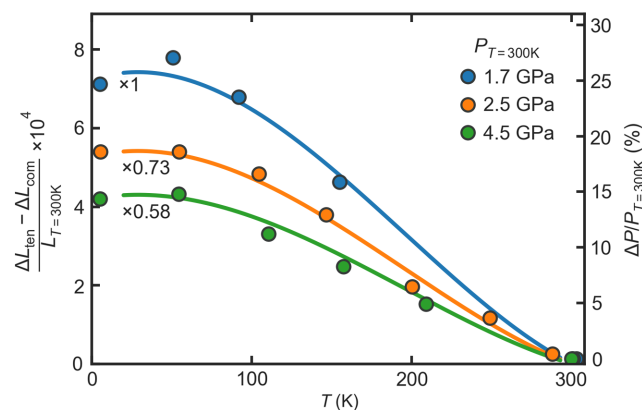


Figure 8. Temperature dependence of the relative difference between the change in length of cell parts that are under tension and the cell parts that are in compression (lines), compared with the relative pressure change P/P_{300K} (circles) at 3 different pressures $P_{T=300K}$, taken from Figure 7. The change in length of the cell parts is obtained by taking into account the cell dimensions, as shown in Figure 9, and the thermal expansion of the different materials obtained from Ref. [114–116]. An arbitrary normalizing coefficient is used to scale this line to the 3 data sets obtained at different pressures.

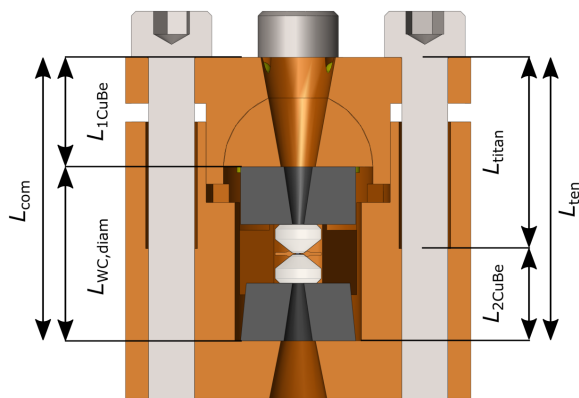


Figure 9. Cross-section of DAC 2 shown in Figure 4. The central part of the cell is under compression when load is applied, with a total length L_{com} comprised of a section made of copper beryllium $L_{1\text{CuBe}}$ and a section made of WC and diamond $L_{\text{WC,diam}}$. The part of the cell that is under tension, with length L_{ten} , is composed of the load screws from the head to the point where they meet the thread in the bottom cell body L_{titan} , and the portion of the bottom cell body down to where the anvil seats rest $L_{2\text{CuBe}}$.

contraction at each pressure. The relative change of dimension was proportional to the relative increase of pressure, except for a load-dependent coefficient. Moreover, as expected the pressure change decreases under increasing loads. This behavior strongly suggested that the difference in the thermal expansion of the various components of the cell is the dominating factor in the change of pressure with temperature in these type of cells. Similar results are also observed in other studies.^[17]

The hysteretic behavior shown in Figure 7, namely that the pressure is always higher after the cooling cycle, was strongly reminiscent of the behavior of the pressure when increasing and decreasing the load on a DAC at room temperature. After a small increase of the load, parts of the gasket were deformed plastically and do not recover the initial shape, thus the final pressure after recovering the initial load was slightly higher than the initial pressure.^[25] It seems plausible that after each temperature cycle the pressure change with temperature becomes smaller for the same reasons observed in small load cycles.

2.4. Neutron Depolarization Under Pressure

Investigating magnetic materials under large pressures was challenging. The use of induction techniques in high-pressure cells is often prohibitively difficult as the signal due to the very small samples is much smaller than the background produced by the surrounding pressure cell. Optical or transport techniques are also difficult to implement, and only offer indirect information on the magnetic properties.

In comparison, neutron depolarization (ND) offers the possibility to determine accurately the transition temperature of the sample and obtain an estimate of the evolution of the magnetic moment and domain size, even inside a pressure cell. Neutrons readily penetrate cryogenic equipment and can access the sample through the optical aperture of the cell body. The diamond or moissanite anvils, through which the beam is transmitted, have

a small neutron absorption while they leave the polarization of neutrons unchanged.

In an ND experiment, the change of the polarization of a polarized neutron beam is analyzed after transmission through the sample. During transmission, the neutron spin and thus the polarization vector of a neutron beam was affected by the local magnetization of the medium undergoing Larmor precession. The decrease of the beam polarization when traversing a ferromagnet was first described theoretically by Halpern and Holstein in 1941.^[26] As a neutron traverses a Heisenberg ferromagnet at a velocity v , it spends an average time τ inside each domain of average size δ , with $\tau = \delta/v$. Assuming an internal magnetic induction B , and random orientation of the domain direction, successive Larmor precessions occur with respect to different field directions across the sample. For a sample thickness d , which is assumed to be much larger than the mean domain size δ , and assuming that the time spent inside a domain is much smaller than the time required for a full Larmor precession, i.e. $\tau \ll 1/\gamma B$, the beam polarization P_f may be expressed as

$$P_f = P_0 \exp\left(-\frac{1}{3}\gamma^2 B^2 d \delta / v^2\right) \quad (5)$$

where P_0 is the initial beam polarization. The main parameters that play a role in the depolarization values are the magnetic field inside a domain, the distance traveled by the neutron across the sample (sample thickness), the mean domain size, and the neutron velocity. More details on the theoretical and experimental aspects of neutron depolarization can be found in Ref. [27].

Considering the 60 m thickness limitation in the sample space of our DACs, the signal amplitude was expected to drop considerably as compared to conventional ND experiments with sample sizes of the order of a few millimeters. Additionally, ND experiments suffered from poor spatial resolution and long integration times. To mitigate the poor spatial resolution, the collimation of the neutron beam may be increased at the expense of the neutron flux at the sample position. As a consequence, to achieve good counting statistics with reasonable integration times, the highest resolution achieved in ND was about 0.5 mm,^[28,29] which was larger than the sample space available in DACs.

These limitations may be overcome with the use of neutron optics.^[30] Neutron guides with a parabolic curvature using a neutron supermirror coating may be used to focus the neutron beam into a small cross-section to significantly increase the neutron flux at the sample position.^[31–33] For the studies, it was designed and constructed a focusing neutron module allowing ND measurements under pressure to be performed routinely at the beamline ANTARES of the Heinz Maier-Leibniz Zentrum (MLZ) neutron source.^[34,35]

The working principle of this enhanced ND experiment is shown in Figure 10. A pair of parabolic neutron guides was placed in confocal geometry. The incoming polarized neutron beam was thus condensed at the focal point where the sample space of the pressure cell was placed. Following the transit through the sample, the neutron trajectories were highly divergent. They were refocused and transmitted to the analyzer and detector with the help of the second guide.

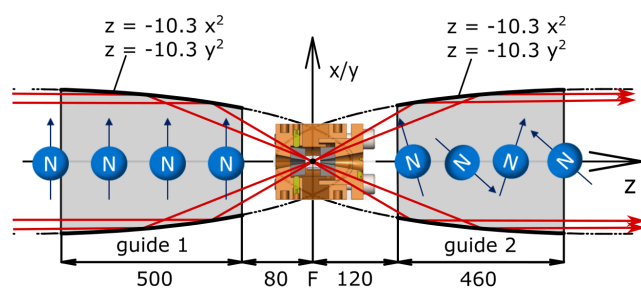


Figure 10. Schematic depiction of the enhanced ND experiment under high pressure. A pair of parabolic neutron supermirror guides (gray area) share the same focal point (F), where the sample space of a DAC is placed. The red arrows exemplify trajectories of the incoming polarized neutron beam. The values given are in millimeter. The drawing is not to scale.

The guides had a square cross-section and a parabolic curvature along the direction of the neutron beam. Unlike what may be suggested in the schematic depiction shown in Figure 10, the guides were very long as compared to their cross-section. The reflection angles were rather small, ranging from 0.37° to 0.99° . The inside of the focusing guide was covered with an $m = 6$ nickel/titanium (Ni/Ti) supermirror coating, giving a maximum reflection angle of about 3° for neutrons with a wavelength of 5 \AA .

This way, the neutron flux at the sample space was increased by two orders of magnitude, leading to a gain of integrated intensity by a factor of 20 at the detector as compared to a standard ND experiment. With the same exposure time, the experimental accuracy was reduced from a polarization of 2% with standard ND, to less than 0.3% using the parabolic guides. Further technical details on the design and utilization of this module will be reported elsewhere.^[36]

3. Itinerant Ferromagnetism in SrRuO_3

The itinerant ferromagnet SrRuO_3 crystallizes in an orthorhombically distorted perovskite structure with $Pnma$ space group and lattice parameters $a = 5.578 \text{ \AA}$, $b = 5.539 \text{ \AA}$, and $c = 7.842 \text{ \AA}$.^[37] The crystal structure consists of tilted corner-sharing RuO_6 octahedra with strontium ions arranged in between.

Itinerant ferromagnetic order is rarely seen in 4d transition metal compounds based on elements like ruthenium, due to the large overlap of the orbitals. The increased bandwidth leads to a spin splitting of the conduction bands, thus being less favorable to a Stoner instability.^[38] Nonetheless, bulk SrRuO_3 exhibits a second-order phase transition from a paramagnetic to a ferromagnetic state at a Curie temperature of $T_C = 165 \text{ K}$.^[39]

Hydrostatic pressure may increase the hybridization of the orbitals, resulting in a suppression of ferromagnetic order. Since room-temperature X-Ray diffraction studies up to 25.2 GPa reveal no structural phase transition,^[40] SrRuO_3 is an interesting candidate to study quantum phase transitions in an ordered system.^[41,42] Auspiciously, the parent compounds Sr_2RuO_4 and $\text{Sr}_3\text{Ru}_2\text{O}_7$, representing the single- and bi-layer members of the Ruddlesden–Popper series, respectively, show

interesting emergent phenomena. Sr_2RuO_4 is known to be the first layered perovskite compound, not containing copper, displaying unconventional superconductivity.^[43,44] $\text{Sr}_3\text{Ru}_2\text{O}_7$ seems to be in the vicinity of a tricritical point driven by pressure with metamagnetic transitions under an applied magnetic field.^[45,46]

The pressure dependence of the Curie temperature of single-crystalline SrRuO_3 was investigated by Hamlin and coworkers under nearly hydrostatic conditions.^[40] They studied the AC magnetic susceptibility as a function of temperature for different pressures up to 34 GPa, where they found an almost linear decrease of the Curie temperature with a rate of $dT_C/dP = -6.8 \text{ K GPa}^{-1}$ up to 17.2 GPa. At higher pressures, from 20.4 to 34 GPa, the ferromagnetic transition could not be resolved. No evidence of superconductivity was observed above 4 K.

The signal from the ferromagnetic transition of SrRuO_3 observed in the AC susceptibility seemed to significantly decrease at pressures above 10 GPa, becoming very difficult to resolve.^[40] Hamlin et al., therefore, used the third harmonic of the susceptibility, offering a superior signal-to-noise ratio at the highest pressures, to continue tracking the transition. This evolution raised the question of whether the size of the ordered moment decreased with pressure to a point where it was no longer observable in the susceptibility or a different phenomenon, akin to the tricritical wings observed in $\text{Sr}_3\text{Ru}_2\text{O}_7$, takes place. The second scenario seems more likely, representing the generic theoretical predictions for clean itinerant ferromagnets.^[47] We attempted to shed more light on this question using the experimental tools described in the previous sections.

First, we performed high-pressure neutron depolarization measurements on single-crystalline SrRuO_3 samples using the DAC shown in Figure 4.3A,B. Single crystals were grown by the traveling floating zone technique in a mirror furnace and are characterized in Ref. [48,49]. Several measurements were performed at pressures up to 17.1 GPa. These measurements proved to be challenging. The combination of the small spontaneous magnetization of SrRuO_3 and the small sample thickness available in the DAC resulted in a low neutron depolarization, consistent with Equation (5). The use of the parabolic neutron guides allowed us to sufficiently enhance the signal-to-noise ratio to obtain meaningful results.

Figure 11 shows the temperature dependence of the neutron beam polarization due to a SrRuO_3 sample at a pressure of 9.0 GPa. The transition from the paramagnetic state with a fully polarized neutron beam ($P = 1$) to the ferromagnetic state where the beam polarization drops rapidly can clearly be observed. Since the neutron depolarization depends exponentially on the spontaneous magnetization, which is zero in the paramagnetic state and grows continuously in the ferromagnetic state, ND measurements are particularly sensitive for the detection of the Curie temperature. Similar measurements were performed at different pressures, confirming the linear decrease of the Curie temperature with pressure described by Hamlin and coworkers, as highlighted in the pressure–temperature magnetic phase diagram of SrRuO_3 shown in Figure 12.

At 17.1 GPa, no significant signal was observed in the temperature dependence of the polarization down to the lowest temperature studied. Diamond anvils with a smaller culet size (0.5 mm) were used to reach this high pressure, requiring an even smaller

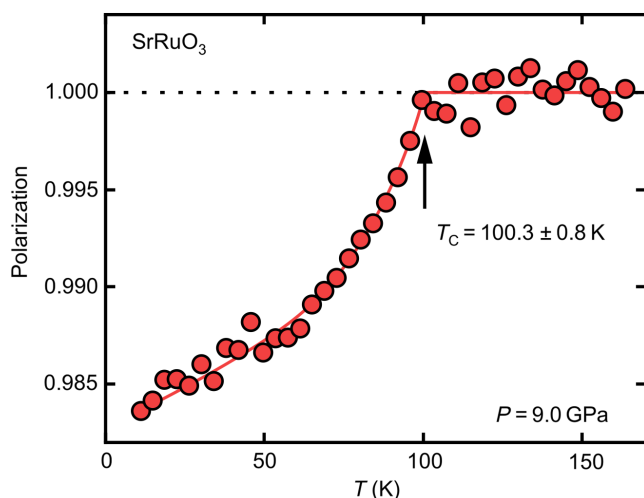


Figure 11. Temperature dependence of the neutron polarization through a SrRuO₃ sample at a pressure $P = 9.0$ GPa. A magnetic guide field of 100 mT was applied. The solid line is a guide to the eye.

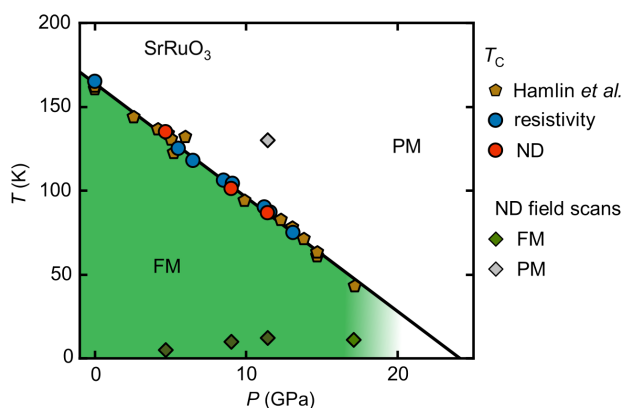


Figure 12. Pressure–temperature magnetic phase diagram of SrRuO₃. The Curie temperature T_C obtained from neutron depolarization (ND) (red circles) and from transport measurements (blue circles) is compared to the values obtained from susceptibility measurements by Hamlin et al. (brown pentagons), reporting a linear decrease of T_C with a slope of $dT_C/dP = -6.8$ K GPa⁻¹ (black line).^[40] Diamonds indicate if a magnetic field scan implied ferromagnetic (FM, green) or paramagnetic (PM, gray) behavior. The ferromagnetic phase is colored in green, fading away for pressures > 17.2 GPa.

sample thickness. It is, therefore, not possible to confirm conclusively if the ferromagnetic order has collapsed at this pressure or the signal is too small to be resolved. However, measurements as a function of the magnetic field, at low temperatures revealed significant hysteresis in the ND signal, suggesting that ferromagnetism is still present at this pressure, maybe as the result of metamagnetic transitions. Further details of these preliminary data are described in Ref. [50].

In addition, resistivity measurements of single-crystalline samples of SrRuO₃ under pressure were performed using the modified Bridgman cell shown in Figure 2. The temperature and magnetic field dependence of the resistivity was measured

at several pressures up to 13 GPa. At all pressures, the resistivity decreased with temperature and a clear change of slope marked the transition from the paramagnetic to the ferromagnetic regime. This feature allowed us to track the Curie temperature as a function of pressure, as shown in Figure 12. No signs of superconductivity were observed above 2 K up to the highest pressures studied. At low temperatures, the resistivity exhibits the T^2 -behavior of a Fermi liquid for all pressures measured. This behavior was confirmed down to a temperature of 200 mK at 9.1 GPa. The dependence of the resistivity on the magnetic field exhibited hysteretic behavior in the ferromagnetic regime without significant changes for different pressures.

These results confirmed the findings of Hamlin et al.,^[40] inferred from the susceptibility. To unequivocally infer the phase diagram of SrRuO₃ at pressures above 17 GPa further experiments are necessary, notably high-pressure resistivity measurements using an improved sample loading technique, as well as high-pressure measurements using nitrogen vacancies as magnetic field sensors.^[51]

4. Incipient Superconductivity in CrB₂

For a long time, it was believed that very high superconducting transition temperatures cannot be reached with conventional electron–phonon interactions. The discovery of superconductivity at the border of long-range magnetic order represents a ubiquitous phenomenon in a wide range of different materials classes that has been attracting great interest as a possible gateway toward very high transition temperatures. Well-known examples comprise the cuprates with their subtle interplay of disorder and unconventional metallic behavior,^[52] the iron arsenides featuring an intricate interplay between superconductivity and density wave order,^[53,54] and f-electron materials with strong electronic correlations.^[55]

On this note, a major surprise has been the discovery of conventional phonon-mediated multi-gap superconductivity with $T_C \approx 39$ K in the hexagonal C32 compound MgB₂. In a series of ultra-high-pressure studies, superconductivity has now been reported in nonmagnetic MoB₂ and WB₂,^[56,57] where T_C was found to reach 32 and 17 K, respectively, at pressures of order ≈ 100 GPa. Moreover, superconductivity was also reported in CrB₂ when itinerant-electron antiferromagnetism is suppressed at pressures above ≈ 15 GPa, where T_C reaches ≈ 7 K at 110 GPa, the highest pressures studied.^[56] As the electronic density of states at the Fermi level of these systems is dominated by the 3d, 4d, or 5d electrons, superconductivity in the transition metal diborides promises to shed new light on the interplay between strong electronic correlations and phonon-mediated pairing in the pursuit of high transition temperatures.

An important agenda of the interplay of magnetism and superconductivity concerns the precise pressure conditions for superconductivity to occur. For instance, changes of sign of dT_C/dP were observed in YBa₂Cu₃O_{7- γ} under quasi-hydrostatic pressure.^[58] Similarly, in BaFe₂As₂ and SrFe₂As₂, an increasing uniaxial pressure component reduced the spin-density wave order more effectively.^[59,60] Further, using steatite powder as a pressure transmitter and different sample orientations, a remarkably strong dependence of the superconducting dome

on non-hydrostatic pressure components was observed in CePd_2Si_2 .^[61] Finally, for tetragonal systems such as PuMGe_5 with $M = (\text{Co}, \text{Rh})$ and CeMIn_5 with $M = (\text{Co}, \text{Rh}, \text{Ir})$, the superconductivity depends sensitively on the ratio of the lattice constants.^[62–64]

As the pressure techniques used to generate ultra-high pressures in the recent studies of MoB_2 , WB_2 , and CrB_2 involved solid rather than liquid pressure transmitters,^[56,56,57] we decided to explore the relationship between lattice anisotropy and superconductivity in CrB_2 in an investigation combining hydrostatic, uniaxial, and quasi-hydrostatic pressures.^[21,65] For our study, we chose the itinerant-electron antiferromagnet CrB_2 with its rather low Néel temperature $T_N = 88\text{K}$, as high-purity single crystals grown by means of optical floating-zone technique were available.^[66–68] The samples investigated under pressure were cut from the same ingots for which the transport and thermodynamic properties as well as quantum oscillatory and neutron scattering studies were reported previously.^[21,69,70]

In our study, three different pressure cells were used, notably a piston–cylinder cell for pressures up to 2.2 GPa, a uniaxial pressure cell for pressures up to 0.5 GPa, and a Bridgman cell for measurements up to 8 GPa. While the piston–cylinder cell allowed to generate hydrostatic pressure conditions, the uniaxial pressure cell served to apply a force along selected crystallographic directions. The uniaxial pressure cell was designed as a scaled-down version of a pressure cell described in Ref. [71], where stainless steel bellows activated by helium gas act on the upper anvil which, in turn, is moved against the fixed lower anvil.^[72,73] Since no-pressure medium is employed, a sample that is placed between both anvils is stressed uniaxially.

Several Cu:Be Bridgman cells were set up using WC and Al_2O_3 anvils in combination with steatite as pressure transmitter and pyrophyllite gaskets. Annealed 25 μm Pt wires were placed on top of the sample and the electrical contacts were established mechanically. As the solid pressure transmitter generated quasi-hydrostatic pressures, i.e., hydrostatic pressure with an additional uniaxial pressure component superimposed, two sample layouts were used as shown in Figure 13. In the first layout shown in Figure 13a, one sample was mounted. This compares with the second layout shown in Figure 13b, in which two

samples were mounted such that the c -axes of the samples were perpendicular and parallel to the direction of the loading force, respectively. The latter was parallel to the line of sight in Figure 13.

For all configurations studied, the same qualitative temperature dependence of the resistivity was observed reminiscent of ambient pressure and characteristic of a good metal. Typical data are shown in Ref. [21,65]. With decreasing temperature, the resistivity decreases monotonically and limits in a small residual value ρ_0 of a few $\mu\Omega\text{cm}$. Around the Néel temperature T_N , the temperature dependence of ρ changes from sublinear to super-linear, where a maximum in the first derivative, $d\rho/dT$, at a temperature T^* slightly below T_N allowed us to track the onset of antiferromagnetism. Under hydrostatic pressures generated with the clamp cell, T^* decreased weakly. In contrast, T^* increased for uniaxial pressure applied in the hexagonal basal plane, while it decreased strongly for uniaxial pressure applied along the hexagonal c axis. Yet, taking into account the compressibility, all three pressure dependences prove to be consistent with a dependence of T^* on the ratio of lattice constants.

As shown in Figure 14, an unexpected observation in the measurements under quasi-hydrostatic pressures represents the emergence of a drop of the resistivity below $T_c \approx 2\text{K}$ in samples oriented such that the c axis was parallel to the loading force and thus in the presence of an additional uniaxial pressure component. No such drop of the resistivity was observed for the second sample with a rotated orientation, as shown in Figure 14b. An applied magnetic field of the order of 10T suppresses the drop in the resistivity. Moreover, the absolute values of T_c as well as the rate of suppression of T_c under magnetic field, dT_c/dH are quantitatively consistent with the recent report of a full superconducting transition of the resistivity at ultra-high pressures.^[56] In turn, we interpret the drop in the resistivity as incipient superconductivity.

Using the dependence of T^* on the change of the ratio of lattice constants $\Delta(c/a)$ observed at low pressures, the data recorded under quasi-hydrostatic pressures was analyzed, yielding the phase diagram shown in Figure 15. Decreasing $\Delta(c/a)$ results in a gradual suppression of itinerant-electron antiferromagnetism as tracked by means of T^* and a concomitant

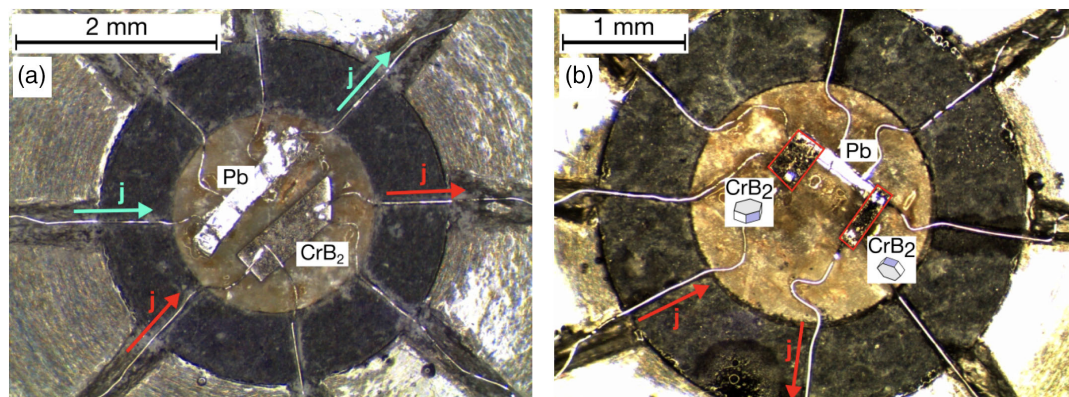


Figure 13. Top view of the anvils of the Bridgman cells as prepared with single-crystal CrB_2 . Electrical press contacts were made using 25 μm Pt wire. A Pb strip was used as a superconducting manometer. a) Setup with a single CrB_2 sample (bc-1). b) Setup with two samples of crossed orientation, where the c axis was parallel and perpendicular to the line of sight, respectively (bc-2).

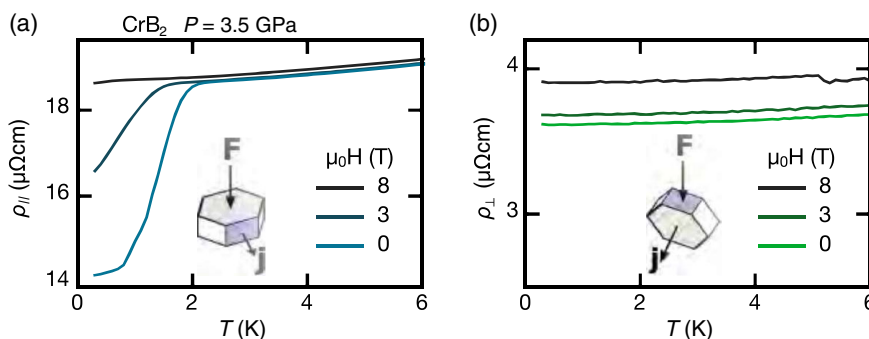


Figure 14. Typical temperature dependence of the electrical resistivity of the two CrB₂ samples shown in Figure 13b measured simultaneously at a pressure of 3.5 GPa. Putative evidence is observed for incipient superconductivity for a decreasing ratio of the lattice constants. a) Resistivity for load parallel to the *c* axis. The decrease of the resistivity below $T_c \approx 2$ K is suppressed under moderate magnetic fields. b) Resistivity for load parallel to the *a*-axis, where no drop in the resistivity is observed.

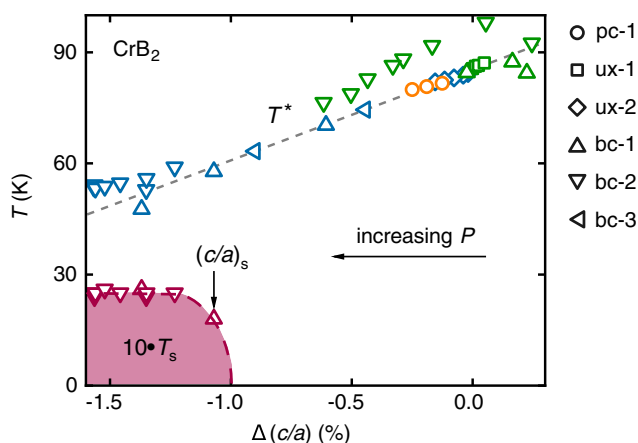


Figure 15. Phase diagram of CrB₂ showing characteristic temperatures as a function of the change of the ratio of lattice constants $\Delta(c/a)$. Data are shown as inferred from measurements using a clamp cell (pc-1), uniaxial pressure cell using a He-activated bellow system (ux-1, ux-2), and quasi-hydrostatic Bridgman cells (bc-1, bc-2, bc-3). The response of T^* recorded under uniaxial and hydrostatic pressures establishes quantitatively that T^* varies with $\Delta(c/a)$. Using this relationship for T^* the emergence of incipient superconductivity under quasi-hydrostatic pressures may be inferred.

emergence of superconductivity in CrB₂. This behavior suggests that the magnetism and superconductivity as observed under ultra-high pressures in CrB₂ originates in a change of $\Delta(c/a)$ rather than the unit cell volume. In the search for those components of the quasi-particle interactions that drive the superconductive pairing, this finding promises to become a cornerstone that may ultimately allow to identify the microscopic details of the interplay of itinerant antiferromagnetism and superconductivity in CrB₂.

5. Magneto-Elastic Coupling in CeCuAl₃

In recent years, paramagnetic rare-earth intermetallics with sizeable magneto-elastic interactions have attracted increasing interest. In these studies a well-defined multiplet structure of

the f-electrons^[74] allowed to track the interplay of crystal electric fields (CEFs) with the spectrum of phonons. Representing one of the first examples, seminal studies reported a vibronic bound state (VBS) between phonons and CEF excitations in CeAl₂.^[75–78] Similar VBSs have also been proposed for PrNi₂,^[79] Ce₃Pt₂₃Si₁₁,^[80] and CePd₂Al₂.^[81,82] In contrast, an anti-crossing, representing a different magneto-elastic coupling, has been suggested between acoustic phonons and CEF excitations in Pr and PrAl₂ under an applied magnetic field as well as in the magnetically ordered state of VO₄. While the latter are mediated by dipolar interactions,^[83–88] a generic anticrossing in zero magnetic field that is mediated by quadrupolar interactions may have been observed in PrAlO₃,^[89] TbVO₄,^[90] and PrNi₅.^[91,92] Further, the lifetime and temperature dependence of CEF excitations, which deviates in many materials from the thermal population of single-ion states,^[93–98] has been attributed to interactions with particle-hole excitations in metallic systems.^[99] These interactions may be responsible for superconductive pairing^[55] as observed in UPd₂Al₃^[96,97,100,101] and PrOs₄Sb₁₂.^[102]

In this field of research, the series of CeTAl₃ (*T* = Ce, Au, Pd, Pt) compounds,^[103,104] which are part of the wider family of BaAl₄-type systems, has been attracting increasing interest. Inspired by studies on CePd₂Al₂, neutron spectroscopy in polycrystalline as well as single-crystal CeCuAl₃ revealed a VBS.^[105–107] Considering hybridization with optical phonons, which results in four doublets $|\Gamma_6, 0\rangle$, $|\Gamma_6, 1\rangle$, and $|\Gamma_{12}, 0\rangle$, these studies suggested early on that the symmetry of lattice fluctuations results in a different character of VBSs in a tetragonal environment as compared to cubic systems such as CeAl₂.

Systematic time-of-flight neutron spectroscopy in polycrystalline CeRhGe₃^[108,109] CeAuAl₃ failed to detect a VBS. In addition, an exploratory search for magneto-elastic phonon softening in CeCuAl₃ and CeAuAl₃ by means of inelastic X-ray scattering was also inconclusive.^[110] Yet, high-precision neutron spectroscopy in single-crystal CeAuAl₃ revealed two pronounced magneto-elastic hybrid excitations beyond the Born–Oppenheimer approximation.^[111,112] Namely, a vibronic bound state and a well-resolved anticrossing. As an additional surprise, both excitations involved acoustic instead of optical phonons, with considerable damping due to the coupling to particle-hole excitations even though the coupling constants are small.

In the light of the increasing number of materials featuring spectroscopic evidence for pronounced magneto-elastic coupling effects, the application of high pressures appears to be a natural tuning parameter. However, as spectroscopic studies under high pressures tend to be prohibitively difficult, indirect evidence for changes of the magneto-elastic coupling may be inferred from the transport measurements. For instance, strong interactions between phonons and CEFs have been identified from additional contributions to the thermal conductivity in CeAuAl_3 .^[113] This finding suggests that even the electrical resistivity may be sensitive to magneto-elastic interactions.

Motivated by the spectroscopic evidence for magneto-elastic interactions in CeCuAl_3 and CeAuAl_3 , we studied the electrical resistivity of single-crystal CeCuAl_3 under pressure. As the characteristic energy scales of the magneto-elastic coupling and the VBS are moderately high, the focus of our study concerned changes of the properties at intermediate temperatures. In fact, it was unfortunately not possible to track the pressure dependence of the antiferromagnetic transition in CeCuAl_3 in our resistivity data.

For our study, single crystals were grown by means of the optical floating-zoning technique.^[66,67] Bridgman pressure cells as described earlier were used with steatite as a pressure transmitter. To track the effects of putative anisotropies of the applied pressure, two samples with crossed crystallographic orientation were mounted in the pressure cell, as shown in **Figure 16**.

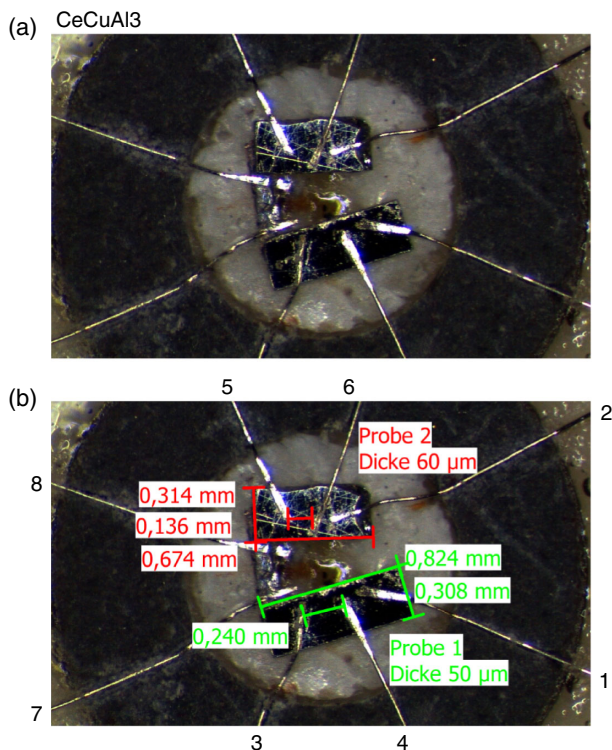


Figure 16. Top view of the anvil of the Bridgman cell as prepared for simultaneous measurements of two CeCuAl_3 samples in a crossed orientation, where the c axis was parallel and perpendicular to the line of sight for Samples 1 and 2, respectively. Electrical press contacts were made using 25 μm Pt wire. A Pb strip was used as a superconducting manometer. Both panels show the same photograph for the sake of clarity.

Sample 1 was oriented such that the line of sight was parallel to the $\langle 001 \rangle$ axis and current applied along the $\langle 100 \rangle$ axis, while Sample 2 was oriented such that the line of sight was parallel to the $\langle 100 \rangle$ axis and current applied along the $\langle 001 \rangle$ axis (in **Figure 16b** Samples 1 and 2 are denoted Probes 1 and 2, respectively). As depicted in **Figure 16b**, the electrical contacts were organized such that two current leads (1,2) were used with the samples arranged in series. The voltage contacts (3,4), (5,6), and (7,8) were connected to Sample 1, Sample 2, and the Pb strip, respectively.

Shown in **Figure 17a,b** is the resistivity as a function of temperature for selected pressures for samples 1 and 2, i.e., for currents applied along $\langle 100 \rangle$ and $\langle 001 \rangle$, respectively. We have no evidence for possible systematic errors such as changes of the geometry factor (e.g., due to microcracks or a mechanical shift of voltage contacts). With increasing pressure up to 6 GPa, the same qualitative changes are observed for both current directions, indicating that CeCuAl_3 is insensitive to possible pressure anisotropies as well as the direction in which the electrical resistivity was measured.

The main changes of resistivity under pressure may be summarized as follows. The absolute value of the resistivity increases by roughly a factor of two. Under increasing pressure, the featureless monotonic decrease of the resistivity developed a broad maximum around 80 K. In addition, below roughly 20 K a pronounced peak developed at several Kelvin followed by a fairly pronounced decrease towards lower temperatures. As shown in **Figure 17c,d** for the resistivity as normalized to its value at 60 K, the relative increase toward the peak at several Kelvin was rather pronounced and of the order 15%. Application of a magnetic field up to 9 T perpendicular to the direction of the electrical current suppressed the peak, as highlighted in **Figure 17c,d** but did not affect the broad maximum in the resistivity around 80 K (not shown).

A temperature dependence of the resistivity that is characteristic of a metallic state at the lowest temperatures studied followed by a pronounced peak under increasing temperature provides evidence of the emergence of strong incoherent electronic correlations, putatively featuring a heavy Fermi liquid ground state and strong Kondo lattice fluctuations. The pressure-induced appearance of such characteristics in CeCuAl_3 , which are suppressed in turn under an applied magnetic field, points at an increase of the hybridization between the conduction electrons and the magnetic degrees of freedom as compared to a mere broadening of the conduction bands observed in itinerant-electron magnets.

Moreover, the emergence of the broad maximum around 80 K suggests an increase of the coupling between the CEFs and phonons under pressure. Within experimental accuracy, however, the temperature at which this maximum emerges appears to be unchanged, consistent with the notion that neither the optical phonons nor the CEF is dispersive. In turn, to leading order, we expect that high pressures in CeCuAl_3 induce changes in the lifetimes of the CEF excitations rather than changes of the spectra themselves.

As a corollary, this finding implies that large pressures allow to tune the interplay between the conduction electrons and magneto-elastic degrees of freedom, while magneto-elastic modes such as the VBS change only weakly. This conjecture

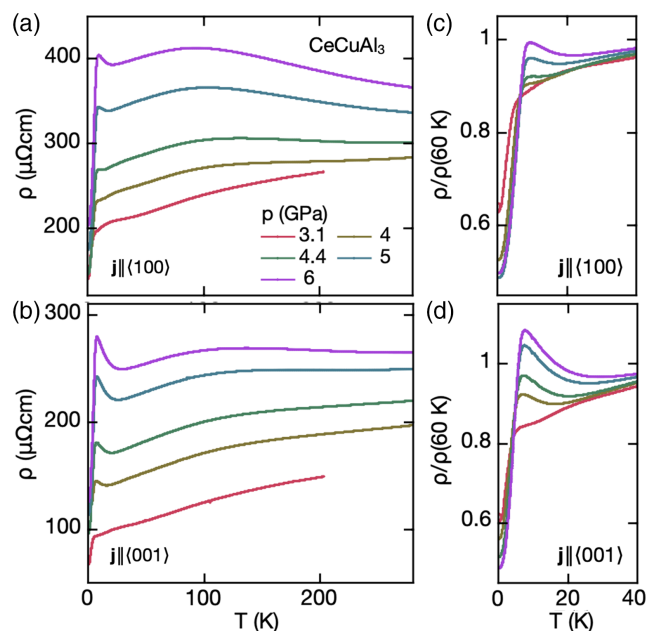


Figure 17. Electrical resistivity of CeCuAl_3 at zero magnetic field as measured simultaneously for two sample orientations with respect to the direction of the applied load. a) Resistivity for the load parallel to $\langle 001 \rangle$ and current parallel to $\langle 100 \rangle$. b) Resistivity for the load parallel to $\langle 100 \rangle$ and current parallel to $\langle 001 \rangle$. c,d) Relative temperature dependence as normalized to the resistivity at 60 K.

highlights an interesting route toward new types of quasiparticle states and quasiparticle interactions, including the possible formation of new forms of electronic order such as unconventional superconductivity.^[55]

6. Challenges and Future Directions

In this review, we presented recent advances in high-pressure instrumentation and measurement techniques. The improved design of the Bridgman cell featuring PCD anvils has allowed us to perform resistivity measurements under pressures above 10 GPa. Three compact DACs were designed and built which could reach pressures as high as 9 and 17 GPa, with moissanite and diamond anvils, respectively. Additionally, we have characterized the pressure change due to thermal expansion in one of the DACs with an in situ measurement of ruby fluorescence. Finally, we built a setup for neutron depolarization measurements under high pressure featuring parabolic neutron guides.

We demonstrated the potential of these high-pressure techniques with studies on three materials. First, high-pressure neutron depolarization measurements using the DACs, and resistivity measurements with the modified Bridgman cell, were used to investigate the suppression of ferromagnetic order under high pressure in SrRuO_3 . Second, incipient superconductivity under quasi-hydrostatic pressure was observed in the itinerant antiferromagnet CrB_2 by means of electrical resistivity measurements. Third, the pressure dependence of the magneto-elastic

coupling in the rare-earth compound CeCuAl_3 was explored with electrical resistivity measurements.

Ongoing efforts are now focusing on the understanding of the suppression of ferromagnetic order in SrRuO_3 up to 17 GPa. For this purpose, the sample loading technique using a solid pressure medium for the electrical resistivity measurements under pressure is being revisited. Additionally, we are building an experimental setup to use the fluorescence of nitrogen vacancies in diamond as highly sensitive magnetic field sensors embedded in the diamond anvils of DACs.^[51]

Acknowledgements

The authors wish to thank Peter Böni, Petr Cermak, Stuart Gilder, Malte Grosche, Sven Friedemann, Andrew Huxley, Anna Kusmartseva, Gil Lonzarich, Philipp Niklowitz, Kai Grube, and Karl Syassen for fruitful discussions and support with the experiments. This work has been funded by the Deutsche Forschungsgemeinschaft (DFG, German Research Foundation) under TRR80 (From Electronic Correlations to Functionality, Project No. 107745057, Project F2), DFG-GACR grant WI3320/3-1 (Project No. 323760292), CRC 1238 (Project No. 277146847, Project A02), and the excellence cluster MCQST under the German Excellence Strategy EXC-2111 (Project No. 390814868). Financial support by the European Research Council (ERC) through Advanced Grants No. 291079 (TOPFIT) and No. 788031 (ExQuiSid) is also gratefully acknowledged.

Open Access funding enabled and organized by Projekt DEAL.

Conflict of Interest

The authors declare no conflict of interest.

Keywords

diamond anvil cells, extreme conditions, magnetism, neutron depolarization, pressure, quantum phase transitions, superconductivity

Received: December 2, 2021

Revised: February 24, 2022

Published online: March 29, 2022

- [1] C. Pfleiderer, G. J. McMullan, S. R. Julian, G. G. Lonzarich, *Phys. Rev. B* **1997**, 55, 8330.
- [2] M. Vojta, *Rep. Prog. Phys.* **2003**, 66, 2069.
- [3] Y. Shimizu, D. Braithwaite, B. Salce, T. Combier, D. Aoki, E. N. Hering, S. M. Ramos, J. Flouquet, *Phys. Rev. B* **2015**, 91, 125115.
- [4] N. D. Mathur, F. M. Grosche, S. R. Julian, I. R. Walker, D. M. Freye, R. K. W. Haselwimmer, G. G. Lonzarich, *Nature* **1998**, 394, 39.
- [5] A. Huxley, I. Sheikin, E. Ressouche, N. Kernavanois, D. Braithwaite, R. Calemczuk, J. Flouquet, *Phys. Rev. B* **2001**, 63, 144519.
- [6] T. Park, V. A. Sidorov, F. Ronning, J. X. Zhu, Y. Tokiwa, H. Lee, E. D. Bauer, R. Movshovich, J. L. Sarrao, J. D. Thompson, *Nature* **2008**, 456, 366.
- [7] R. Ritz, M. Halder, M. Wagner, C. Franz, A. Bauer, C. Pfleiderer, *Nature* **2013**, 497, 231.
- [8] Y. Wang, T. F. Rosenbaum, A. Palmer, Y. Ren, J. W. Kim, D. Mandrus, Y. Feng, *Nat. Commun.* **2018**, 9, 2953.
- [9] M. I. Eremets, *High Pressure Experimental Methods*, Oxford University Press, Oxford, **1996**.

- [10] A. Dewaele, P. Loubeyre, F. Occelli, O. Marie, M. Mezouar, *Nat. Commun.* **2018**, 9, 1.
- [11] A. Jayaraman, *Rev. Mod. Phys.* **1983**, 55, 65.
- [12] J. A. Xu, H. K. Mao, *Science* **2000**, 290, 783.
- [13] D. J. Dunstan, I. L. Spain, *J. Phys. E: Sci. Instrum.* **1989**, 22, 913.
- [14] J. A. Xu, H. K. Mao, R. J. Hemley, E. Hines, *Rev. Sci. Instrum.* **2004**, 75, 1034.
- [15] K. Ullrich, Thesis, University of Cologne, **1980**.
- [16] J. Thomasson, Y. Dumont, J. C. Griveau, C. Ayache, *Rev. Sci. Instrum.* **1997**, 68, 1514.
- [17] S. Yomo, S. W. Tozer, *J. Phys.: Conf. Ser.* **2010**, 215, 012181.
- [18] P. Jorba, PhD Thesis, Technical University of Munich, **2021**.
- [19] K. Syassen, *High Pressure Res.* **2008**, 28, 75.
- [20] G. J. Piermarini, S. Block, J. D. Barnett, R. A. Forman, *J. Appl. Phys.* **1975**, 46, 2774.
- [21] A. Regnat, PhD Thesis, Technical University of Munich, **2019**.
- [22] F. Sigger, B. Sc. Thesis, Technical University of Munich, **2013**.
- [23] K. Nakano, Y. Akahama, Y. Ohishi, H. Kawamura, *Jpn. J. Appl. Phys.* **2000**, 39, 1249.
- [24] A. R. Rosenfeld, B. L. Averbach, *J. Appl. Phys.* **1956**, 27, 154.
- [25] I. L. Spain, D. J. Dunstan, *J. Phys. E: Sci. Instrum.* **1989**, 22, 923.
- [26] O. Halpern, T. Holstein, *Phys. Rev.* **1941**, 59, 960.
- [27] P. Schmakat, PhD Thesis, Technical University of Munich, **2016**.
- [28] N. Kardjilov, A. Hilger, I. Manke, M. Strobl, M. Dawson, J. Banhart, *Nucl. Instrum. Methods Phys. Res. A* **2009**, 605, 13.
- [29] M. Schulz, A. Neubauer, S. Masalovich, M. Mühlbauer, E. Calzada, B. Schillinger, C. Pfleiderer, P. Böni, *J. Phys.: Conf. Ser.* **2010**, 211, 012025.
- [30] P. Jorba, M. Schulz, D. S. Hussey, M. Abir, M. Seifert, V. Tsurkan, A. Loidl, C. Pfleiderer, B. Khaykovich, *J. Magn. Magn. Mater.* **2019**, 475, 176.
- [31] T. Hils, P. Boeni, J. Stahn, *Physica B* **2004**, 350, 166.
- [32] P. Böni, *Nucl. Instrum. Methods Phys. Res. A* **2008**, 586, 1.
- [33] T. Adams, G. Brandl, A. Chacon, J. N. Wagner, M. Rahn, S. Mühlbauer, R. Georgii, C. Pfleiderer, P. Böni, *Appl. Phys. Lett.* **2014**, 105, 123505.
- [34] E. Calzada, F. Gruenauer, M. Mühlbauer, B. Schillinger, M. Schulz, *Nucl. Instrum. Methods Phys. Res. A* **2009**, 605, 50.
- [35] M. Schulz, B. Schillinger, *J. Large-Scale Res. Facil.* **2015**, 1, 17.
- [36] P. Jorba, M. Schulz, M. Seifert, V. Tsurkan, P. Böni, C. Pfleiderer, Magnetic shielding effect and trapped flux in sub-millimeter size superconductors observed with enhanced neutron depolarization, unpublished **2022**.
- [37] SrRuO₃ crystal structure: Datasheet from PAULING FILE in: Inorganic Solid Phases, SpringerMaterials (online database), Springer, Heidelberg **2016**.
- [38] E. C. Stoner, *Proc. R. Soc. London A* **1938**, 165, 372.
- [39] G. Koster, L. Klein, W. Siemons, G. Rijnders, J. S. Dodge, C. B. Eom, D. H. Blank, M. R. Beasley, *Rev. Mod. Phys.* **2012**, 84, 253.
- [40] J. J. Hamlin, S. Deemyad, J. S. Schilling, M. K. Jacobsen, R. S. Kumar, A. L. Cornelius, G. Cao, J. J. Neumeier, *Phys. Rev. B* **2007**, 76, 014432.
- [41] S. Sachdev, in *Handbook of Magnetism and Advanced Magnetic Materials*, Cambridge University Press, Cambridge **2011**.
- [42] M. Brando, D. Belitz, F. M. Grosche, T. R. Kirkpatrick, *Rev. Mod. Phys.* **2016**, 88, 025006.
- [43] Y. Maeno, H. Hashimoto, K. Yoshida, S. Nishizaki, T. Fujita, J. G. Bednorz, F. Lichtenberg, *Nature* **1994**, 372, 532.
- [44] Y. Maeno, S. Kittaka, T. Nomura, S. Yonezawa, K. Ishida, *J. Phys. Soc. Jpn.* **2012**, 81, 011009.
- [45] M. Chiao, C. Pfleiderer, S. R. Julian, G. G. Lonzarich, R. S. Perry, A. P. Mackenzie, Y. Maeno, *Physica B* **2002**, 312–313, 698.
- [46] A. P. Mackenzie, J. A. N. Bruin, R. A. Borzi, A. W. Rost, S. A. Grigera, *Physica C: Supercond.* **2012**, 481, 207.
- [47] D. Belitz, T. R. Kirkpatrick, J. Rollbühler, *Phys. Rev. Lett.* **2005**, 94, 247205.
- [48] S. Kunkemöller, F. Sauer, A. A. Nugroho, M. Braden, *Cryst. Res. Technol.* **2016**, 51, 299.
- [49] S. Kunkemöller, D. Brüning, A. Stunault, A. A. Nugroho, T. Lorenz, M. Braden, *Phys. Rev. B* **2017**, 96, 220406.
- [50] M. Seifert, PhD Thesis, Technical University of Munich, **2021**.
- [51] J. J. Hamlin, B. B. Zhou, *Science* **2019**, 366, 1312.
- [52] S. Chakravarty, R. B. Laughlin, D. K. Morr, C. Nayak, *Phys. Rev. B* **2001**, 63, 094503.
- [53] M. Rotter, M. Tegel, D. Johrendt, *Phys. Rev. Lett.* **2008**, 101, 107006.
- [54] M. Rotter, M. Tegel, D. Johrendt, I. Schellenberg, W. Hermes, R. Pöttgen, *Phys. Rev. B* **2008**, 78, 020503.
- [55] C. Pfleiderer, *Rev. Mod. Phys.* **2009**, 81, 1551.
- [56] C. Pei, J. Zhang, Q. Wang, Y. Zhao, L. Gao, C. Gong, S. Tian, R. Luo, Z. Y. Lu, H. Lei, K. Liu, Y. Qi, Pressure-induced Superconductivity at 32 K in MoB₂, arXiv:2105.13250, **2021**.
- [57] J. Lim, A. C. Hire, Y. Quan, J. S. Kim, S. R. Xie, R. S. Kumar, D. Popov, C. Park, R. J. Hemley, J. J. Hamlin, R. G. Hennig, P. J. Hirschfeld, G. R. Stewart, Creating superconductivity in WB₂ through pressure-induced metastable planar defects, arXiv:2109.11521, **2021**.
- [58] J. S. Schilling, S. Klotz, in *Physical Properties of High Temperature Superconductors III* (Ed: D. M. Ginsberg), World Scientific, Singapore, **1992**, p. 59.
- [59] W. J. Duncan, O. P. Welzel, X. F. Wang, X. H. Chen, F. M. Grosche, P. G. Niklowitz, *J. Phys.: Condens. Matter* **2010**, 22, 1.
- [60] H. Kotegawa, T. Kawazoe, H. Sugawara, K. Murata, H. Tou, *Phys. Soc. Jpn.* **2009**, 78, 083702.
- [61] A. Demuer, A. T. Holmes, D. Jaccard, *J. Phys.: Condens. Matter* **2002**, 14, 529.
- [62] E. D. Bauer, J. D. Thompson, J. L. Sarrao, L. A. Morales, F. Wastin, J. Rebizant, J. C. Griveau, P. Javorsky, P. Boulet, E. Colineau, G. H. Lander, G. R. Stewart, *Phys. Rev. Lett.* **2004**, 93, 147005.
- [63] F. Wastin, P. Boulet, J. Rebizant, E. Colineau, G. H. Lander, *J. Phys.: Condens. Matter* **2003**, 15, S2279.
- [64] P. G. Pagliuso, C. Petrovic, R. Movshovich, D. Hall, M. F. Hundley, J. L. Sarrao, J. D. Thompson, Z. Fisk, *Phys. Rev. B* **2001**, 64, 100503.
- [65] A. Regnat, A. Bauer, A. Deyerling, J. Spallek, J. Becker, A. Chacón, R. Ritz, C. G. F. Blum, S. Gottlieb-Schönmeyer, S. Wurmehl, P. G. Niklowitz, M. A. Wilde, C. Pfleiderer, Emergence of Incipient Superconductivity in CrB₂ under Anisotropic Strain, unpublished, **2021**.
- [66] A. Neubauer, J. Boeuf, A. Bauer, B. Russ, H. V. Löhneysen, C. Pfleiderer, *Rev. Sci. Instrum.* **2011**, 82, 013902.
- [67] A. Bauer, G. Benka, A. Regnat, C. Franz, C. Pfleiderer, *Rev. Sci. Instrum.* **2016**, 87, 013902.
- [68] A. Bauer, G. Benka, A. Neubauer, A. Regnat, A. Engelhardt, C. Resch, S. Wurmehl, C. G. F. Blum, T. Adams, A. Chacon, R. Jungwirth, R. Georgii, A. Senyshyn, B. Pedersen, M. Meven, C. Pfleiderer, *Phys. Status Solidi B* **2021**, 15, 2100159.
- [69] A. Bauer, A. Regnat, C. G. F. Blum, S. Gottlieb-Schönmeyer, B. Pedersen, M. Meven, S. Wurmehl, J. Kuneš, C. Pfleiderer, *Phys. Rev. B* **2014**, 90, 064414.
- [70] M. Brasse, L. Chioncel, J. Kuneš, A. Bauer, A. Regnat, C. G. F. Blum, S. Wurmehl, C. Pfleiderer, M. A. Wilde, D. Grundler, *Phys. Rev. B* **2013**, 88, 155138.
- [71] C. Pfleiderer, E. Bedin, B. Salce, *Rev. Sci. Instrum.* **1997**, 68, 3120.
- [72] S. Waffenschmidt, C. Pfleiderer, H. V. Löhneysen, *Phys. Rev. Lett.* **83**, 3005 (1999).
- [73] A. Schade, T. Adams, A. Chacón, R. Georgii, C. Pfleiderer, P. Böni, *Phys. Rev. B* **2019**, 100, 035122.
- [74] J. H. Mentink, M. I. Katsnelson, M. Leshchko, *Phys. Rev. B* **2019**, 99, 064428.

- [75] M. Loewenhaupt, B. D. Rainford, F. Steglich, *Phys. Rev. Lett.* **1979**, 42, 1709.
- [76] M. Loewenhaupt, U. Witte, *J. Phys.: Condens. Matter* **2003**, 15, S519.
- [77] P. Thalmeier, P. Fulde, *Phys. Rev. Lett.* **1982**, 49, 1588.
- [78] P. Thalmeier, *J. Phys. C: Solid State Phys.* **1984**, 17, 4153.
- [79] E. Mühle, E. A. Goremychkin, I. Natkaniec, *J. Magn. Magn. Mater.* **1989**, 81, 72.
- [80] C. Opagiste, R. M. Galéra, M. Amara, C. Paulsen, S. Rols, B. Ouladdiaf, *Phys. Rev. B* **2011**, 84, 134401.
- [81] L. C. Chapon, E. A. Goremychkin, R. Osborn, B. D. Rainford, S. Short, *Physica B* **2006**, 378–380, 819.
- [82] M. Klicpera, M. Boehm, P. Dolezal, H. Mutka, M. M. Koza, S. Rols, D. T. Adroja, I. Puente Orench, J. Rodriguez-Carvajal, P. Javorský, *Phys. Rev. B* **2017**, 95, 085107.
- [83] P. Thalmeier, B. Lüthi, in *Handbook on the Physics and Chemistry of Rare Earths* (Eds: K. A. Gschneidner, L. Eyring), Vol. 14, Elsevier, Amsterdam **1991**, p. 225.
- [84] J. Jensen, A. R. Mackintosh, *Rare Earth Magnetism*, Clarendon Press, Oxford **1991**.
- [85] H. G. Purwins, W. J. L. Buyers, T. M. Holden, E. C. Svensson, *AIP Conf. Proc.* **1976**, 29, 259.
- [86] J. G. Houmann, B. D. Rainford, J. Jensen, A. R. Mackintosh, *Phys. Rev. B* **1979**, 20, 1105.
- [87] P. Thalmeier, P. Fulde, *Z. Phys. B* **1975**, 22, 359.
- [88] J. K. Kjems, W. Hayes, S. H. Smith, *Phys. Rev. Lett.* **1975**, 35, 1089.
- [89] R. J. Birgeneau, J. K. Kjems, G. Shirane, L. G. Van Uiter, *Phys. Rev. B* **1974**, 10, 2512.
- [90] M. T. Hutchings, R. Scherm, S. H. Smith, S. R. P. Smith, *J. Phys. C* **1975**, 8, L393.
- [91] V. Aksenov, E. Goremychkin, E. Mühle, T. Frauenheim, W. Bührer, *Physica B+C* **1983**, 120, 310.
- [92] M. Reiffers, K. Flachbart, A. B. Beznosov, *Czech. J. Phys. B* **1988**, 38, 197.
- [93] J. M. Lawrence, S. M. Shapiro, *Phys. Rev. B* **1980**, 22, 4379.
- [94] M. Loewenhaupt, J. M. Carpenter, C. K. Loong, *J. Magn. Magn. Mater.* **1985**, 52, 245.
- [95] K. Hense, E. Gratz, H. Nowotny, A. Hoser, *J. Phys.: Condens. Matter* **2004**, 16, 5751.
- [96] E. Blackburn, A. Hiess, N. Bernhoeft, G. H. Lander, *Phys. Rev. B* **2006**, 74, 024406.
- [97] K. Iwasa, K. Saito, Y. Murakami, H. Sugawara, *Phys. Rev. B* **2009**, 79, 235113.
- [98] K. Iwasa, K. Saito, Y. Murakami, H. Sugawara, *J. Phys.: Conf. Ser.* **2010**, 200, 012071.
- [99] K. W. Becker, P. Fulde, J. Keller, *Z. Phys. B* **1977**, 28, 9.
- [100] N. K. Sato, N. Aso, K. Miyake, R. Shiina, P. Thalmeier, G. Varelogiannis, C. Geibel, F. Steglich, P. Fulde, T. Komatsubara, *Nature* **2001**, 410, 340.
- [101] P. Thalmeier, *Eur. Phys. J. B* **2002**, 27, 29.
- [102] E. D. Bauer, N. A. Frederick, P. C. Ho, V. S. Zapf, M. B. Maple, *Phys. Rev. B* **2002**, 65, 100506.
- [103] C. Franz, Ph.D. thesis, Technical University of Munich, **2014**.
- [104] C. Franz, A. Senyshyn, A. Regnat, C. Duvinage, R. Schönmann, A. Bauer, Y. Prots, L. Akselrud, V. Hlukhyi, V. Baran, C. Pfleiderer, *J. Alloys Compd.* **2016**, 688, 978.
- [105] D. T. Adroja, A. del Moral, C. de la Fuente, A. Fraile, E. A. Goremychkin, J. W. Taylor, A. D. Hillier, F. Fernandez-Alonso, *Phys. Rev. Lett.* **2012**, 108, 216402.
- [106] M. Klicpera, D. T. Adroja, K. Vlaskova, M. Boehm, H. Mutka, B. Ouladdiaf, T. Guidi, P. Javorsky, *Inorg. Chem.* **2017**, 56, 12839.
- [107] M. Klicpera, M. Boehm, P. I. Javorský, Investigation of vibron states in a CeCuAl₃ single crystal. Institut Laue Langevin Experimental Report 4-01-1464, **2015**, <https://userclub.ill.eu/userclub/>.
- [108] A. D. Hillier, D. T. Adroja, P. Manuel, V. K. Anand, J. W. Taylor, K. A. McEwen, B. D. Rainford, M. M. Koza, *Phys. Rev. B* **2012**, 85, 134405.
- [109] D. T. Adroja, C. de la Fuente, A. Fraile, A. D. Hillier, A. Daoud-Aladine, W. Kockelmann, J. W. Taylor, M. M. Koza, E. Burzur, F. Luis, J. I. Arnaudas, A. del Moral, *Phys. Rev. B* **2015**, 91, 134425.
- [110] S. Tsutsui, K. Kaneko, J. Pospisil, Y. Haga, *Physica B* **2017**, 536, 24.
- [111] B. Q. Liu, P. C. Cermák, C. Franz, C. Pfleiderer, A. Schneidewind, *Phys. Rev. B* **2018**, 98, 174306.
- [112] P. Cermák, A. Schneidewind, B. Liu, M. M. Koza, C. Franz, R. Schönmann, O. Sobolev, C. Pfleiderer, *Proc. Natl. Acad. Sci. USA* **2019**, 116, 6695.
- [113] Y. Aoki, M. A. Chernikov, H. R. Ott, H. Sugawara, H. Sato, *Phys. Rev. B* **2000**, 62, 87.
- [114] R. J. Corruccini, J. J. Gniewek, *Thermal Expansion of Technical Solids at Low Temperatures: A Compilation from the Literature*, U.S. Gov. Printing Office, Washington D.C. **1961**.
- [115] A. D. Krawitz, D. G. Reichel, R. Hitterman, *J. Am. Ceram. Soc.* **1989**, 72, 515.
- [116] *Thermal Conductivity 24: Thermal Expansion 12: Joint Conferences* (Eds: P. S. Gaal, D. E. Apostolescu), Technomic Pub. Co, Pittsburgh, Pennsylvania, USA **1999**.



Pau Jorba was born in 1988, he obtained a diploma in physics at the University of Barcelona in 2012, and completed a master's degree at the École Polytechnique Fédérale de Lausanne in 2014. Since then he has been working in the group of Christian Pfleiderer at the Technical University of Munich, recently finishing his Ph.D. on the evolution of magnetism in transition-metal compounds under extreme conditions. Besides the development of high-pressure techniques, his research interests include the emergent properties of quantum materials, such as spin-liquid behavior or unconventional superconductivity.



Astrid Schneidewind was born in 1964, and received her diploma and Ph.D. from TU Dresden. After a postdoc at LMU Munich, she moved to the neutron source FRM II, where she is in charge of the cold-neutron triple-axis spectrometer PANDA since 2004. She has run the instrument for the TU Dresden, the Helmholtz-Zentrum Berlin, and currently for the Jülich Center for Neutron Science at MLZ. Her research interests range from magnetic properties and unconventional superconductivity in rare-earth materials, to exotic magnetic ground states and hybridized excitations. She also engages in improving the research by extending digitization supporting the wider neutron community.



Christian Pfleiderer was born in 1965, studied physics in Tübingen and Denver, and received his Ph.D. from the University of Cambridge in 1994. After working as a postdoctoral researcher at the CEA Grenoble and as head of a Helmholtz Junior University Research Group in Karlsruhe, he was appointed at the Technical University of Munich as an associate professor of Magnetic Materials in 2004 and Full Professor of the Topology of Correlated Systems in 2014. He received the 2004 Academy Award of the Heidelberg Academy of Sciences, the 2016 Max Born Prize, and the 2016 Europhysics Prize of the Condensed Matter Division of the European Physical Society.